The Complex Way to Laser Diode Spectra: Example of an External Cavity Laser With Strong Optical Feedback

Original
The Complex Way to Laser Diode Spectra: Example of an External Cavity Laser With Strong Optical Feedback / Detoma, E., B., T., Montrosset, I.. - In: IEEE JOURNAL OF QUANTUM ELECTRONICS. - ISSN 0018-9197. - STAMPA. - 41:(2005), pp. 171-182. [10.1109/JQE.2004.839705]

Publisher:
IEEE-INST ELECTRICAL ELECTRONICS ENGINEERS INC, 445 HOES LANE, PISCATAWAY, NJ 08855-4141 USA

Published
DOI:10.1109/JQE.2004.839705

The Complex Way to Laser Diode Spectra: Example of an External Cavity Laser Strong Optical Feedback

Enrico Detoma, Bjarne Tromborg, and Ivo Montrosset, *Member, IEEE*

***Abstract*—An external cavity laser with strong grating-filtered feedback to an antireflection-coated facet is studied with a time-domain integral equation for the electric field, which reproduces the modes of the oscillation condition as steady-state solutions. For each mode, the stability and spectral behavior is determined by analysis of the location of side modes in the complex frequency plane. The complex frequency diagrams are shown to be a useful tool to determine the self-stabilization effect of mode coupling and its dependence on laser parameters and external cavity design. The model is used to simulate the large signal time evolution after start from unstable modes.**

***Index Terms*—External cavity, four-wave mixing, mode coupling, optical feedback, semiconductor lasers.**

I. INTRODUCTION

IN THIS PAPER, we study the static and dynamic properties of a Fabry–Pérot laser diode with an antireflection (AR)-coated facet and strong optical feedback from an external grating to the facet (see Fig. 1). This kind of external cavity laser (ECL) system finds applications where single-mode output is required over a broad range of wavelengths with narrow linewidth, high side-mode suppression ratio (SMSR), and without mode hopping. The applications include its important use as tunable laser source in optical communications, sensor applications and spectroscopy. If the combined laser cavity includes a saturable absorber, the system may operate as a mode-locked laser and serve as an optical pulse generator. This mode of operation will not be discussed here, but the formalism can easily be generalized to include mode-locking.

The ECL has been the subject of a vast number of publications. We refer to the review article [1] for an extensive list of references (see [2] for more recent references). Most of the theoretical papers on ECLs deal with laser diodes with weak to moderate feedback and are focussed on the particularly rich nonlinear dynamics of these laser systems. If we disregard the work on mode-locking, there have been surprisingly few papers addressing the dynamics of laser diodes with strong and filtered optical feedback and with an external cavity that is much longer than the active region. The papers [3]–[9] are some of the exceptions. The ECL with short external cavity operates in much the same way as a DBR laser on which there is a comprehensive literature. However, the ECL with long external cavity is from a theoretical point of view a qualitatively different system because the gain section can, to a good approximation, be considered as a lumped section, and the narrow mode spacing makes mode coupling a more important mechanism.

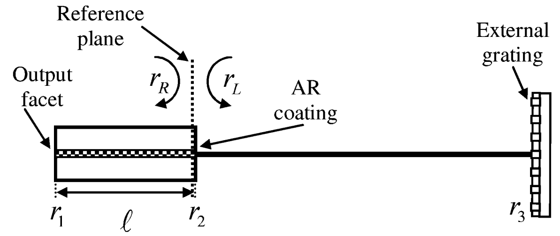

Fig. 1. Structure of the external cavity laser.

The purpose of the present paper is to perform a detailed theoretical investigation of the effect of mode coupling, due to four-wave mixing (FWM), on the stability properties of the longitudinal modes of the ECL composite cavity. This "self-stabilization" effect was analyzed in [3], [8], [10]–[13]. We show that a stability analysis of each longitudinal mode of the ECL can be easily performed in the frequency domain, and we support our claim through the use of complex frequency diagrams which show how stability is affected by bias current and mode detuning from the frequency of the peak of the external reflectivity. The complex frequency diagrams can also help to understand the dynamical effects of mode coupling on the noise spectra. In particular, we give a precise explanation of the appearance of a double-peaked relative intensity noise (RIN) spectrum [14], [15] in terms of small-signal self-oscillations, whose frequency can be quantitatively identified in the complex frequency diagrams. The method of complex frequency diagrams is a way to precisely determine the location and strength of the side modes of a mode, which can be applied to other laser systems.

Complementary to the complex frequency diagrams for the stability, we developed a time-domain model that can be used to analyze the evolution of both stable and unstable modes. The time-domain model consists of an integral equation for the electrical field, with steady-state solutions that coincide with the conventional solutions to the oscillation condition. The use of the integral equation avoids the frequency cutoff that is intrinsic in the usual differential rate equations. This feature leads to an excellent agreement between the spectra obtained with the frequency-domain and the time-domain models for stable modes over a large range of frequencies. In addition, the time-domain model is the only available tool to study the rich dynamics of an unstable mode, which range from limit cycle to chaos but may also end up in mode hops to stable modes.

Manuscript received July 21, 2004; revised September 21, 2004. This work was supported by the BIGBAND Project under the EU-IST 5th Framework Programme.

E. Detoma and I. Montrosset are with the Politecnico di Torino, Dipartimento di Elettronica e PhotonLab, 10129 Torino, Italy (e-mail: enrico.detoma@polito.it).

B. Tromborg is with the Research Center COM, Technical University of Denmark, DK 2800 Lyngby, Denmark.

Digital Object Identifier 10.1109/JQE.2004.839705

The paper is organized as follows. Section II presents the locus curve method for finding the modes of an ECL at and above threshold. Section III contains the small-signal analysis which determines the stability properties of a given mode in terms of the location of zeros of the system determinant in the complex frequency plane. The analysis is illustrated by a specific example for which the frequency tuning range of stable operation is calculated as a function of the bias current. A time-domain integral equation for the field is derived and simulated noise spectra are compared to small-signal spectra. In Section IV, the time-domain model is used to study the large signal dynamics and to illustrate the route to chaos and mode hopping by numerical simulations. Appendix gives details of the noise model and the way to eliminate the singularities which appear in the field power spectrum to first order in the noise diffusion constant.

II. MODES OF AN EXTERNAL CAVITY LASER

The structure of the external cavity laser is shown in Fig. 1. The output facet to the left is assumed to be cleaved while the chip facet to the right is assumed to be AR coated. The external reflector is a selective grating which provides filtered optical feedback over a small range of frequencies.

Referring to Fig. 1, r_1 and r_2 are, respectively, the amplitude reflectivity of the output cleaved facet and that of the AR-coated facet. $r_3(\omega)$ represents the frequency-dependent reflectivity of the external grating that will be modeled by a Lorentzian equation

$$r_3(\omega) = \frac{r_g}{1 + j((\omega - \omega_g)/\Delta\omega)} \tag{1}$$

where r_g is the amplitude reflectivity peak at the angular frequency ω_g, and $\Delta\omega$ provides the filter bandwidth.

The laser operates in the strong feedback regime because the residual reflectivity r_2 of the AR-coated facet is taken to be much smaller than the external reflectivity r_g.

The frequency-domain analysis of the device starts from the laser field equation [13]

$$[1 - r_R(\omega) r_L(\omega, N, P)] \mathcal{E}(\omega) = \mathcal{F}(\omega) \tag{2}$$

where $\mathcal{E}(\omega)$ is the right travelling electric field at the reference plane of Fig. 1, which is chosen to be at and to the left of the AR-coated facet. $\mathcal{F}(\omega)$ is a noise term that represents the spontaneous emission added to the optical field during a round trip in the diode, and $r_R(\omega)$ and $r_L(\omega, N, P)$ are the right and the left effective reflectivities seen at the reference plane. The left effective reflectivity, which represents the round-trip of the field through the gain medium, depends on the carrier density N and the photon number P in the chip cavity.

The expression for the right reflectivity derives directly from the scattering matrix for a Fabry–Pérot etalon

$$r_R(\omega) = \frac{r_2 + r_3(\omega) e^{-j\omega\tau}}{1 + r_2 r_3(\omega) e^{-j\omega\tau}} \tag{3}$$

where τ is the round-trip time in the external cavity.

The expression for the left reflectivity depends on the length ℓ of the active laser cavity and on the propagation constant k

$$r_L(\omega, N, P) = r_1 e^{-2j\ell k(\omega, N, P)}. \tag{4}$$

The propagation constant k in the laser cavity is given by the following expression:

$$k(\omega, N, P) = \frac{\omega}{c} n(\omega, N, P) + j\frac{1}{2}[g(\omega, N, P) - \alpha_i] \tag{5}$$

where n is the modal refractive index, g is the modal gain, and α_i is the internal loss coefficient.

Equation (2) gives the following oscillation condition in absence of noise:

$$r_R(\omega) r_L(\omega, N, P) = 1 \tag{6}$$

whose solutions, represented by points in the (ω, N) plane, are the steady states or the modes of the external cavity laser. The set of ECL modes lie on the locus curve(s) that the modes follow in the (ω, N) plane when the length of the external cavity is varied. It was shown in [4] that the locus curve is an effective tool to get an overview of the location of the ECL modes for varying laser parameters.

A. Locus Curve

In this subsection, we show how to derive the locus curve and discuss a specific example.

By inserting (3) in (6) and rearranging the terms, the oscillation condition can be written in the form

$$1 - r_L(\omega, N, P) r_2 = r_3(\omega)(r_L(\omega, N, P) - r_2) e^{-i\omega\tau}. \tag{7}$$

The same equation can be obtained more directly by choosing the reference plane to lie to the right of the AR-coated facet.

The locus curve is obtained by taking the absolute value of both sides of (7) and, thereby, eliminating the dependence on the external cavity round-trip time τ

$$|1 - r_L(\omega, N, P) r_2| = |r_3(\omega)(r_L(\omega, N, P) - r_2)|. \tag{8}$$

Since (7) is equivalent to (6), the locus curves lie between the lower and upper boundaries given by $|r_L| r_{R\max} = 1$ and $|r_L| r_{R\min} = 1$ in the plane (ω, N), where $r_{R\max} = (r_2 + |r_3|)/(1 + r_2|r_3|)$ and $r_{R\min} = (r_2 - |r_3|)/(1 - r_2|r_3|)$.

The left reflectivity r_L is dealt with in the following way. We choose a reference frequency ω_0 and a reference carrier density N_0 by solving the oscillation condition (6) at the threshold ($P = 0$) with the assumption that the right facet reflectivity is constant and equal to the maximum of r_R, which we call r_m

$$r_1 r_m e^{-2j\ell k(\omega_0, N_0)} = 1 \tag{9}$$

with

$$r_m = \frac{r_2 + r_g}{1 + r_2 r_g}. \tag{10}$$

The choice of such a reference frequency is natural because we are mainly interested in studying the ECL modes that see the highest right reflectivity, thus being the most obvious candidates for lasing. In addition, the search of solutions to (6) in the plane (ω, N) is numerically simplified by the choice of a reference frequency near the operating point.

Using (4) and (9), the following expression for the left reflectivity is obtained:

$$r_L(\omega, N, P) = \frac{e^{-2j\ell\Delta k(\omega,N,P)}}{r_m} \tag{11}$$

where

$$\begin{aligned} 2\ell\Delta k(\omega, N, P) &= 2\ell\left[k(\omega, N, P) - k(\omega_0, N_0)\right] \\ &\simeq \tau_{\text{in}}\hat{\omega} - \phi_0 + j\ell(1+j\alpha)\frac{\partial g}{\partial N}\Delta N + j\ell\frac{\partial g}{\partial P}P. \end{aligned} \tag{12}$$

In this equation, α is the linewidth enhancement factor, and τ_{in} is the internal cavity round-trip time given by $\tau_{\text{in}} = 2\ell/v_g$, where v_g is the group velocity. We also introduced the variables $\hat{\omega} = \omega - \omega_g$, $\Delta N = N - N_0$ and $\phi_0 = \tau_{\text{in}}(\omega_0 - \omega_g)$. The absolute value of ϕ_0 is in practice unknown, but we know to some approximation how ω_0, and hence ϕ_0, tunes with bias current and temperature. The reflector bandwidth $\Delta\omega$ is assumed to be small compared to the gain bandwidth, so we ignore the frequency dependence of the gain and use $g(\omega, N_0, 0) = g(\omega_0, N_0, 0)$. To simplify the following discussion, the normalized carrier density $\hat{N} = \ell(\partial g/\partial N)\Delta N$ is introduced.

As an example we consider the configuration of Fig. 1 with a laser chip of length 500 μm. The length of the external cavity in air is 11 cm. The spacing of the compound cavity modes amounts to $\approx$ 1.3 GHz and is similar to that of the device analyzed in [15], while the laser chip is longer in our case. We choose to simulate an imperfect AR coating whose power reflectivity is $r_2^2 = 5 \cdot 10^{-3}$. This is the value that can easily be obtained over a broad wavelength range ($\approx$ 200 nm) with current AR coating technique without using tilted waveguides or window structures. It can, therefore, be regarded as a worst case condition for this kind of devices. The external reflector is a selective grating with maximum power effective reflectivity $r_g^2 = 0.34$ and a full width at half maximum (FWHM) of $\Delta\omega/\pi = 20$ GHz. We shall first ignore the nonlinear gain, i.e., the dependence of the modal gain on the active region photon number P.

The laser parameters are shown in Table I. With this choice of parameters, there is a family of locus curves depending on the parameter ϕ_0, all of which lie between the upper and lower boundaries given by the dashed curves in Fig. 2. The vertical axis is the normalized carrier density $\hat{N}$, and the frequency axis is $\hat{\omega}/2\pi$. The dash-dotted lines are the lines for which the phase of r_L is $m\pi$ for integer m, i.e., they are given by

$$\hat{N} = \frac{\tau_{\text{in}}\hat{\omega} - \phi_0 + m\pi}{\alpha}. \tag{13}$$

For even/odd m, the lines intersect the locus curve where it touches the lower/upper boundaries. The lines sweep with varying ϕ_0; Fig. 2(a) and (b) show two examples of choice of ϕ_0, where the low-threshold ECL modes closely follow the lower [Fig. 2(a)] and upper [Fig. 2(b)] limits. The modes are shown as bullets on the locus curve for a specific choice of the cavity length. They move like pearls on a string toward lower frequencies when the cavity length is increased.

TABLE I
LASER PARAMETERS

Parameter	Value	Description
α	4	Linewidth enhancement factor
ℓ	500 μm	Laser chip length
v_g	$9.4 \cdot 10^7$ m $\cdot$ s^{-1}	Group velocity in laser chip
$\partial g/\partial N$	$4.3 \cdot 10^{-17}$ cm^2	Differential gain
$\partial g/\partial P$	$-3.6 \cdot 10^{-6}$ cm^{-1}	Gain saturation factor
α_i	9 cm^{-1}	Internal losses
τ_s	0.5 ns	Carrier lifetime
V_c	$1.44 \cdot 10^{-10}$ cm^3	Volume of the active region
n_{sp}	2	Population inversion factor
r_2^2	$5 \cdot 10^{-3}$	AR coating power reflectivity
r_g^2	0.34	Maximum external power reflectivity
r_1^2	0.3	Output facet power reflectivity

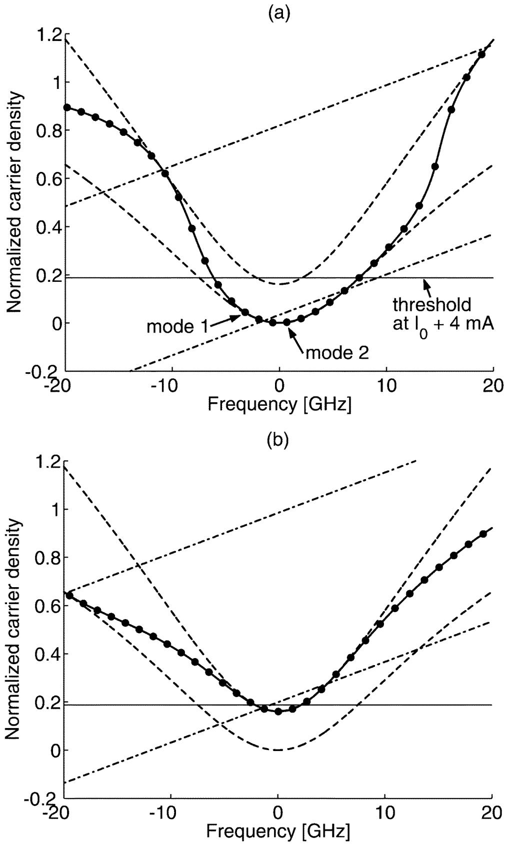

Fig. 2. Example of two different locus curves (solid), depending on the parameter ϕ_0, for an ECL with imperfect AR coating. The bullets represent the ECL modes. The vertical axis is the normalized carrier density $\hat{N}$, and the frequency axis is $\hat{\omega}/2\pi$. Both locus curves lie within two boundaries given by the maximum and the minimum of the right reflectivity r_R (dashed). The locus curves touch the boundaries where they intersect the dash–dotted lines, which represent a phase condition, (13), for the left reflectivity r_L. In both figures, a horizontal line shows the normalized threshold carrier density given by (17) for 4-mA bias current above the minimum threshold current I_0.

Fig. 2 shows the location of the ECL modes at threshold. In order to describe the steady states above threshold, we need to introduce the carrier rate equation. In the time domain, it reads

$$\frac{dN}{dt} = \frac{I}{qV_c} - \frac{N}{\tau_s} - v_g g\left(N, P\right)\frac{P}{V_c} \tag{14}$$

where I is the injected current, q the elementary charge, V_c the volume of the active region, and τ_s the carrier lifetime. The corresponding steady-state equation can then be written as

$$\frac{I - I_0}{q} = \frac{V_c \Delta N}{\tau_s} + (\gamma + V_c G_N \Delta N + G_P P)P \tag{15}$$

where the following parameters are introduced:

$$\gamma = v_g g \quad G_N = v_g \frac{\partial g}{\partial N}\frac{1}{V_c} \quad G_P = v_g \frac{\partial g}{\partial P}. \tag{16}$$

The parameter $I_0 = qV_c N_0/\tau_s$ is the minimum threshold current for any mode. For a given bias current I, (6) and (15) can be solved to give the stationary states $(\hat{\omega}_s, \hat{N}_s, P_s)$. The positions $(\hat{\omega}_s, \hat{N}_s)$ may be slightly shifted compared to their threshold positions due to a nonzero gain compression factor G_P. Furthermore, it is only the solutions with normalized carrier density $\hat{N}_s$ less than

$$\hat{N}_c = (I - I_0)\frac{\tau_s \tau_{\text{in}} G_N}{2q} \tag{17}$$

which have positive P_s and hence are above threshold. Equation (17) is derived from (15) by setting $P = 0$ and making use of the definitions (16). Having determined the modes, which are above threshold, the next problem is to determine their stability properties. It is often assumed that the laser system can only oscillate in the mode with lowest threshold carrier density. However, as we shall see, the mode coupling due to four-wave mixing may also allow the laser system to operate in other modes.

III. LARGE- AND SMALL-SIGNAL DYNAMICS

A. Time-Domain Analysis

In order to study the dynamics of the ECL system, we need to add the information about the dynamics of the carrier density which is lacking in (2). We, therefore, transform the field equation (2) to the time domain and generalize it to apply for time-varying carrier density.

We use (11) and (12) to rewrite the laser field equation (2) in the following form:

$$\left[e^{j\hat{\omega}\tau_{\text{in}}} - \frac{r_R\left(\omega_g + \hat{\omega}\right)}{r_m} e^{j\phi_0 + \ell(1+i\alpha)(\partial g/\partial N)\Delta N + \ell(\partial g/\partial P)P}\right] \times \mathcal{E}\left(\omega_g + \hat{\omega}\right) = \mathcal{F}\left(\omega_g + \hat{\omega}\right) e^{j\hat{\omega}\tau_{\text{in}}}. \tag{18}$$

The separation between the carrier frequency ω_g and the detuning frequency $\hat{\omega}$ allows us to perform an inverse Fourier transform of (18), with $\hat{\omega}$ as the frequency variable. The result is an integral equation for the slowly varying envelope of the electric field $E(t)$

$$E(t) = e^{(1/\tau_{\text{in}}) \int_{t-\tau_{\text{in}}}^{t} [\ell(1+i\alpha)(\partial g/\partial N)\Delta N + \ell(\partial g/\partial P)P] dt'} \times \left(r \otimes E\right)|_{t-\tau_{\text{in}}} + F(t). \tag{19}$$

The symbol "$\otimes$" denotes time-domain convolution, and the function $r(t)$ is the inverse Fourier transform of the ratio $r_R\left(\omega_g + \hat{\omega}\right)\exp\left(j\phi_0\right)/r_m$. It represents the impulse response of the external cavity seen from the reference plane. In the exponential factor, the gain is averaged over a round-trip τ_{in} interval in the active cavity, to better express the mean field nature of $E(t)$.

We normalize the electric field such that $|E(t)|^2$ is the right travelling power at the reference plane. In steady-state operation, the power is proportional to the photon number, with the proportionality constant given by (52) in the Appendix. We assume that this proportionality also holds for nonstationary operation. With this assumption, the time-domain field (19) and the carrier density rate (14) fully determine the dynamics of the ECL system. The field equation expressed as an integral equation has the same steady-state solutions, as we obtain from the oscillation condition (6) and the steady-state carrier rate (15). If we replace t by $t+\tau_{\text{in}}$ in (19) and $E(t+\tau_{\text{in}})$ by $E(t)+\tau_{\text{in}} dE/dt$, the field equation becomes a differential-integral equation of a form that is often used to describe ECL systems. However, the steady states of that equation will not reproduce the modes of the oscillation condition.

A similar approach to the dynamical study of an external cavity laser was employed in [16] and [17].

B. Stability Analysis

For given bias current, the modes $(\hat{\omega}_s, \hat{N}_s, P_s)$ with $\hat{N}_s \leq \hat{N}_c$ are above threshold but they may not all be stable. In order to identify the stable modes, we perform a small-signal analysis of (19) and (14) in the frequency domain [13]. The Fourier transform of $E(t)$ is written as

$$\int_{-\infty}^{\infty} E(t) e^{-j\hat{\omega}t} dt = E_s 2\pi\delta(\tilde{\omega}) + \delta E(\tilde{\omega}) \tag{20}$$

where $\tilde{\omega} = \hat{\omega} - \hat{\omega}_s = \omega - \omega_s$ is the frequency excursion from the steady-state frequency ω_s, and E_s is the steady-state field amplitude. The Fourier transform of the carrier density can be expanded in a similar way, and by insertion in the Fourier transformed (19) and (14), the following equation is obtained:

$$\left[1 - \mathcal{G}\left(\tilde{\omega}\right) + B\left(\tilde{\omega}\right)\right]\delta E\left(\tilde{\omega}\right) + B\left(\tilde{\omega}\right)\delta E^*\left(-\tilde{\omega}\right) = F\left(\omega_s + \tilde{\omega}\right) \tag{21}$$

where

$$\mathcal{G}\left(\hat{\omega}\right) = \frac{r_R\left(\omega_s + \tilde{\omega}\right)}{r_R\left(\omega_s\right)} e^{-j\tilde{\omega}\tau_{\text{in}}} \tag{22}$$

and

$$B(\tilde{\omega}) = \frac{1 - e^{-j\tilde{\omega}\tau_{\text{in}}}}{2j\tilde{\omega}} \times \left\{ \frac{(1+j\alpha)\left[\omega_R^2 + \frac{1}{4}(\Gamma_N - \Gamma_P)^2\right]}{j\tilde{\omega} + \Gamma_N} + \Gamma_P \right\}. \quad (23)$$

We have followed the notation of [18] for the following variables:

$$\omega_R^2 = \gamma G_N P \quad \Gamma_N = \tau_s^{-1} + G_N P \quad \Gamma_P = -G_P P. \quad (24)$$

The parameter ω_R is the relaxation angular frequency, Γ_N is the damping rate of the carrier density, and Γ_P is the damping rate of the photon density which takes into account the nonlinear gain compression.

Another equation can be obtained from (21) by replacing $\tilde{\omega}$ with $-\tilde{\omega}$ and taking the complex conjugate

$$[1 - \mathcal{G}^*(-\tilde{\omega}) + B^*(-\tilde{\omega})]\,\delta E^*(-\tilde{\omega}) + B^*(-\tilde{\omega})\,\delta E(\tilde{\omega}) = F^*(\omega_s - \tilde{\omega}). \quad (25)$$

The system of (21) and (25) can be solved to provide δE as a function of the noise F. They can be written in the following more compact form:

$$\begin{pmatrix} X + B & B \\ B' & X' + B' \end{pmatrix} \begin{pmatrix} E_1 \\ E_2 \end{pmatrix} = \begin{pmatrix} F_1 \\ F_2 \end{pmatrix} \quad (26)$$

with

$$\begin{aligned} X &= 1 - \mathcal{G}(\tilde{\omega}) \quad X' = 1 - \mathcal{G}^*(-\tilde{\omega}) \\ B &= B(\tilde{\omega}) \quad B' = B^*(-\tilde{\omega}) \\ E_1 &= \delta E(\tilde{\omega}) \quad E_2 = \delta E^*(-\tilde{\omega}) \\ F_1 &= F(\omega_s + \tilde{\omega}) \quad F_2 = F^*(\omega_s - \tilde{\omega}). \end{aligned} \quad (27)$$

The solution is

$$\begin{aligned} E_1 &= \frac{F_1(X' + B') - F_2 B}{D} \\ E_2 &= \frac{F_2(X + B) - F_1 B'}{D} \end{aligned} \quad (28)$$

where D is the system determinant

$$D(\tilde{\omega}) = (X + B)(X' + B') - BB'. \quad (29)$$

The first step to determine the stability of the considered mode $(\hat{\omega}_s, \hat{N}_s, E_s)$ is to find the zeroes of the system determinant in the complex frequency plane $\tilde{\omega}$. The zeros correspond to small-signal oscillations, whose imaginary part gives the damping. If one of the zeros has a negative imaginary part, the oscillations are undamped and the mode is unstable; otherwise the mode is stable. The zeros can be found by an approach similar to the locus curve method for solving the oscillation condition [19]. $D(\tilde{\omega})$ is a second-order polynomial in $\exp(j\tilde{\omega}\tau)$, and solving $D(\tilde{\omega}) = 0$ with respect to $\exp(j\tilde{\omega}\tau)$ will, therefore, result in two solutions of the form $\exp(j\tilde{\omega}\tau) = f_i(\tilde{\omega})$, $i = 1, 2$. By taking the norm on both sides of the equation we eliminate the rapidly changing phase factor $\exp(j\mathrm{Re}(\tilde{\omega})\tau)$. The curves $\exp(-\mathrm{Im}(\tilde{\omega})\tau) = |f_i(\tilde{\omega})|$ are, therefore, smooth curves in the complex frequency plane on which the zeros have to lie. The zeros are easily found by searching along the curves.

It is clear from (26) that $B(\tilde{\omega})$ serves as a mode coupling parameter that couples E_1 and E_2. The origin of B is the four-wave mixing due to carrier pulsations and nonlinear gain. It is zero at threshold but, as we shall see, it plays an important role above threshold. When $B(\tilde{\omega})$ can be ignored, we have $D(\tilde{\omega}) = X'X$ and the zeros of $D(\tilde{\omega})$ will, therefore, be solutions to $X = 0$ or $X' = 0$. The equation $X = 0$, i.e., $\mathcal{G}(\tilde{\omega}) = 1$, is simply the oscillation condition for complex frequencies and for fixed carrier density equal to the steady-state value N_s. The solutions to $X' = 0$ will be the mirror image of the zeros of X with respect to the imaginary axis of the $\tilde{\omega}$ plane.

We shall illustrate the stability analysis for the example of Fig. 2(a). Here, two modes are highlighted, at opposite sides with respect to the carrier frequency ω_g. For a bias current of 4 mA above threshold, the result of the analysis is shown in Fig. 3, where in both cases the complex frequency curves $\exp(-\mathrm{Im}(\tilde{\omega})\tau) = |f_i(\tilde{\omega})|$ with mode coupling (solid curves) are compared to the same curves without mode coupling (dashed curves), i.e., for $B = B' = 0$. The bullets show the zeros of $D(\tilde{\omega})$; the zero at the origin represents the considered mode and the other zeros represent the side modes of the mode.

Fig. 3(a) shows that mode 1 of Fig. 2(a), whose frequency is lower than the carrier frequency ω_g, becomes stable due to the effect of mode coupling; all side modes move up in the upper half complex frequency plane as the current increases. On the other hand, mode 2 of Fig. 2(a), whose frequency is higher than ω_g and whose small-signal analysis is shown in Fig. 3(b), becomes more unstable when mode coupling increases.

As mentioned above, the condition $\mathcal{G}(\tilde{\omega}) = 1$, which determines one of the branches for negligible mode coupling, is identical to the oscillation condition (6) for fixed carrier density $N = N_s$ and $P = 0$. This implies that the branch intersects the real axis in the complex $\tilde{\omega}$ plane at frequencies which are identical to the frequencies (relative to $\hat{\omega}_s$) where the line $\hat{N} = \hat{N}_s$ cuts the locus curve in the $(\hat{\omega}, \hat{N})$ plane. Thus, if a horizontal line is drawn through mode 1 in Fig. 2(a), it will intersect the locus curve again at a frequency which is 6.46 GHz above mode 1. In Fig. 3(a), we see that this is also the frequency where the corresponding dashed branch cuts the real axis. The modes with carrier density below mode 1 correspond to side modes on the section of the branch below the real axis. For simple locus curves as those of Fig. 3, this picture holds for all modes and implies that only the mode with lowest threshold carrier density can be stable in the limit of no mode coupling. All other modes will be unstable because their side mode corresponding to the lowest threshold mode will have negative imaginary part. This argument does not necessarily hold for locus curves with vertical tangents as shown in [13, Fig. 4]. The figure exemplifies the mentioned correspondence between modes and side modes.

Generally speaking, the increase of mode coupling creates an asymmetry of the stable range around ω_g, which favors the modes at lower frequencies. This effect is shown in Fig. 4, where the stable range boundaries are plotted versus injection current. For the same device parameters as in Fig. 3 (solid lines), we observe a shift and a strong broadening of the stable range toward

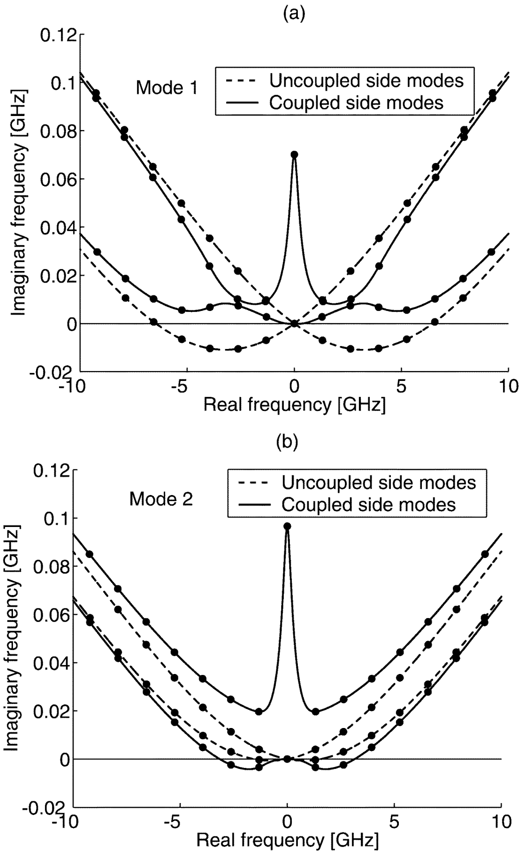

Fig. 3. Complex frequency curves for the highlighted modes of Fig. 2 at 4 mA current above threshold (solid lines) in comparison to the same curves exactly at threshold (dashed lines), i.e., without mode coupling due to four-wave mixing ($B = B' = 0$). Bullets along the curves represent the side modes, i.e., the zeros of the system determinant D of (29). The presence of a side mode with negative imaginary frequency means that the considered mode is unstable. (a) corresponds to the case of a mode with lower frequency than that of the peak of the external reflectivity, where stabilization is due to the effect of mode coupling and stability increases with bias current. (b) corresponds to a mode on the other side of the external reflectivity peak. In this case the increase of bias current leads to reduced stability.

frequencies that are lower than ω_g as current increases. To analyze the effect of gain compression, we performed a calculation where $\partial g/\partial P$ was set equal to zero. When the stabilizing effect of gain compression is not present, the broadening of the stable range is weaker (dashed line).

The circles in Fig. 4 indicate where there are changes of the slope of the lower boundary of the stable tuning range. The slope depends on which side mode creates the instability: before the first circle, the instability is created by the first side mode; but at about 0.4 mA above threshold; it is the second side mode that makes the mode unstable, and we observe a change of slope. From Fig. 3(a), at 4 mA above the threshold, we see that the fourth side mode is about to cross the real axis and create an instability: this is reflected in Fig. 4, where three changes of slope are present before that current level.

The stabilizing effect of mode coupling was first studied by Bogatov *et al.* [10], and it has since been analyzed in a number of articles [3], [8], [11]–[13]. In the recent work by Godard *et al.* [8], it was shown that mode coupling gives a tuning range versus output power similar to Fig. 4, and the results were shown to be in good agreement with experiments. The discussion in [8] also presents a simple physical explanation of the asymmetric tuning range imposed by the combined effect of four-wave mixing and the linewidth enhancement factor.

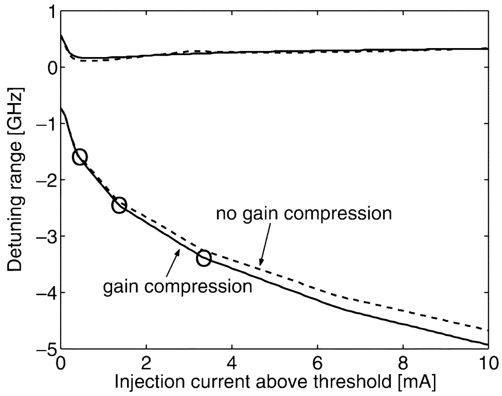

Fig. 4. Stable range around the frequency of the peak of the external reflectivity for increasing current above threshold. The solid curves represent the upper and lower boundaries of the stable range when the simulation is performed with a gain compression term $\partial g/\partial P$ different from zero, while the dashed boundaries were obtained with $\partial g/\partial P = 0$. Gain compression contributes to enlarge the stable range for frequencies lower than ω_g. Three changes of slope are highlighted in the figure: they correspond to changes of the side mode which creates the instability for the lasing mode.

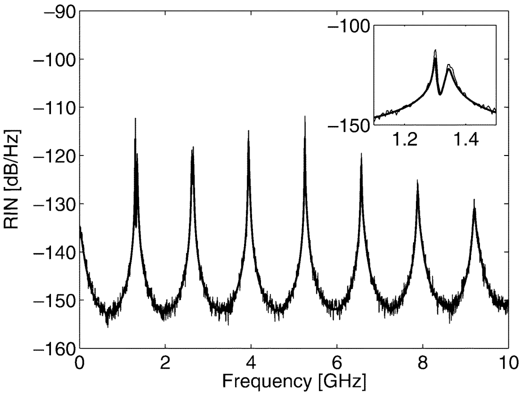

Fig. 5. Relative intensity noise spectrum for the stable mode of Fig. 3(a). The inlet highlights the double peak in correspondence of the first side mode. The small-signal analysis (thick regular curve) is in very good agreement with the time-domain simulation (thin irregular curve), up to very high frequencies (more than 200 GHz, not shown on the current axis scale).

C. Spectral Behavior

In this subsection, we give examples of the small-signal spectral behavior of our ECL system. The derivation of the analytical expressions for the relative intensity noise (RIN), frequency noise and field power spectra are given in the Appendix in (36), (37), and (49). With the device parameters and the stable mode of Fig. 3(a), these equations give the spectra shown in Figs. 5–7 as thick solid lines. The lines are superimposed on the time-domain spectra (irregular thin lines) obtained by numerical simulation of the time-domain equations. The agreement between the two methods is excellent in a large frequency range (more than 200 GHz, not shown), which leaves the time-domain model as a powerful simulation tool for dealing with high-speed communication applications. In both the small-signal calculations and the time-domain simulations, we assume the noise spectrum $S_{\rm sp}(\omega)$ of (34) to be white and equal to $S_{\rm sp}(\omega_s)$. We notice that in our

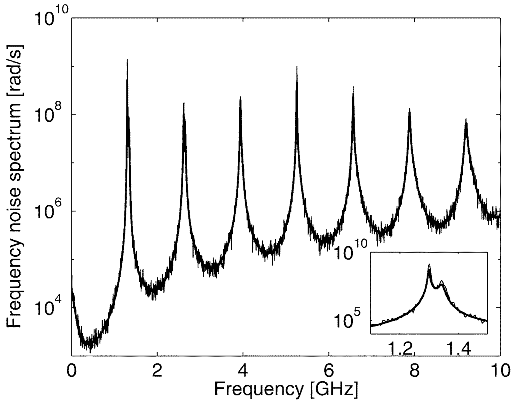

Fig. 6. Frequency noise spectrum for the stable mode of Fig. 3(a).

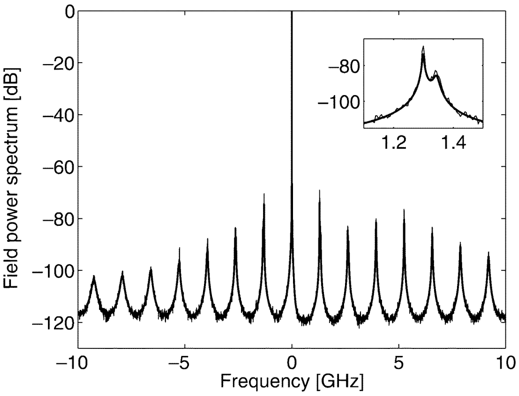

Fig. 7. Normalized field power spectrum $S_E(\tilde{\omega})/S_E(0)$ for the stable mode of Fig. 3(a). The spectrum is not filtered through an optical spectrum analyzer. Thus, the side-mode suppression ratio appears higher than it really is, due to the very narrow linewidth of the lasing mode. In order to calculate the side-mode suppression ratio, one has to integrate over the main and side modes to get the powers in the modes. In this case, the side-mode suppression ratio is about 36 dB.

case the frequency noise spectrum increases as $\tilde{\omega}^2$ beyond the bandwidth of the carrier dynamics until it is finally cut off by the finite bandwidth of $S_{\rm sp}(\omega)$. A white spontaneous emission spectrum will, therefore, give a divergent integral in (42), but we can still apply the white noise assumption if we use the approximation (43). The calculation of the field power spectrum $S_E(\tilde{\omega})$ requires special care to eliminate divergences of phase noise terms at $\tilde{\omega} = 0$. The details of the calculation are given in the Appendix.

The peaks in the spectra in Figs. 5–7 are actually double peaks as highlighted in the inlets for the first side mode at 1.3 GHz. The presence of the double peaks can be traced to the two branches of the solid curve in Fig. 3(a) that both have zeros of the system determinant with real parts close but not equal to multiples of the compound cavity round-trip frequency. The double peaks in the inlets arise from the double zeros representing the first side mode. They correspond to two close small-signal oscillation frequencies which become evident in the spectra.

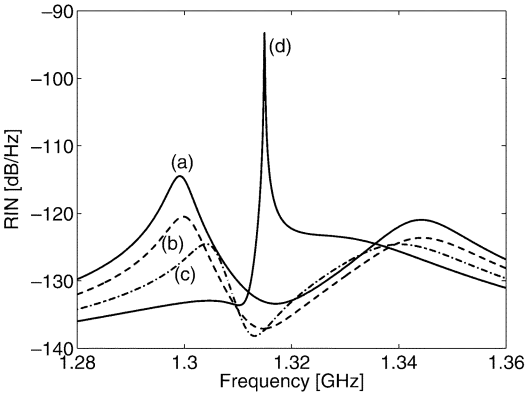

Fig. 8. Evolution of the double-peaked RIN spectrum as the lasing mode is fine tuned from lower to higher frequencies with respect to the external grating reflectivity peak. Starting near the lower boundary of the stable range, (a) shows a high noise peak at about 1.3 GHz followed by a smaller one at about 1.34 GHz. As the lasing mode moves well into the stable range, the first peak drastically decreases (b-c), but a new high and sharper peak appears at about 1.32 GHz as we approach the other boundary at higher frequency than the grating peak (d). The detuning frequencies of the modes which correspond to the curves (a)–(d) are, respectively, -3.58, -2.3, -1.05, and 0.26 GHz (see Fig. 4).

It is interesting to show the evolution of the double peaks of the first side mode as the mode moves in the stable range from negative to positive detuning frequencies with respect to the carrier frequency ω_g. While keeping a current of 4 mA above threshold, we move a stable mode from the lower boundary of Fig. 4 to the upper boundary and we examine the behavior of the double peak of the RIN spectrum. Four different RIN curves along this path are plotted in Fig. 8(a)–(d). When the lasing mode is near the boundary at negative frequencies (a), a high noise peak is present at about 1.3 GHz, followed by a lower peak at about 1.34 GHz. The higher peak is due to the zero of the system determinant which is nearest to the real axis in the complex frequency plane, when looking at the couple of zeros which correspond to the first side mode. As the mode is tuned to higher frequencies inside the stable range, the first peak decreases [Fig. 8(b) and (c)], but when the mode approaches the upper boundary at positive frequencies [Fig. 8(d)], a new high noise peak appears at about 1.32 GHz. For detuning to positive frequencies, the double zeros are pushed away from each other and from the branches for negligible mode coupling [cf. Fig. 3(b)]. The high noise peak will, therefore, sit on top of a broad peak due to the zero with the larger imaginary part. The spectral dip to the left of the high peak is due to a zero in the numerator of the RIN expression (36) [15].

The double-peak behavior has been studied in a number of papers [14], [15], [19], [20]. In [19], the zeros on the two branches in the complex frequency plane were shown to lead to spectral splitting of one of the side modes for an ECL with weak optical feedback. Van Exter *et al.* [15] measured the splitting for negative detuning and showed good agreement with a simple theoretical model. In [20], Ahmed and Tucker presented measurements and theory of intensity modulation spectra for an ECL, which show the same characteristics as our RIN spectra for positive detuning. The splitting of RIN spectra for an ECL were measured over the full stable tuning range by Bogatov *et al.* [14] and were explained as an effect of mode beating. The present study gives an overview of the side-mode behavior under detuning and increase of bias current in terms of complex frequency diagrams.

IV. LARGE-SIGNAL TIME-DOMAIN SIMULATIONS

So far, we analyzed a case where the grating selectivity was high enough to keep single-mode operation with well-suppressed side modes. Now, we will move to another example

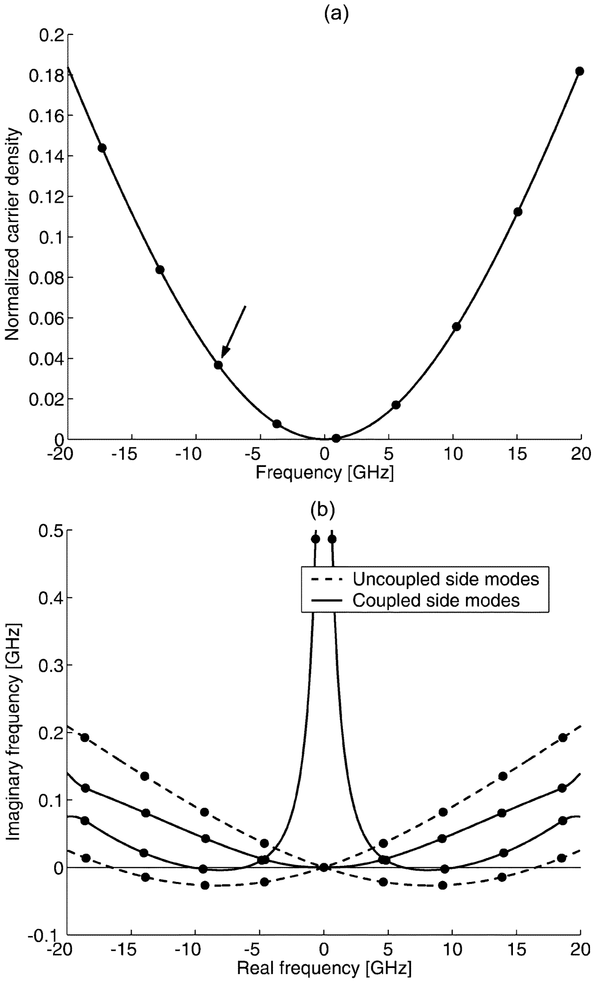

Fig. 9. Locus curve (a) and stability analysis (b) for an ECL with large grating reflectivity bandwidth and high injection current. The frequency axis is $\hat{\omega}/2\pi$ in (a) and $\tilde{\omega}/2\pi$ in (b). The stability analysis is performed for the mode indicated by the arrow. The mode is unstable due to a side mode with slightly negative imaginary frequency.

where a lower selectivity of the external grating allows a range of different dynamical behaviors, when a mode enters the instability region, rather than just performing a mode hop to another stable mode.

Fig. 9 presents the locus curve and the corresponding stability analysis for one of the modes for a case of low grating selectivity (full width at half maximum 60 GHz) and high injection current (80 mA), with perfect AR coating ($r_2 = 0$). In comparison to the previous example, also the mode spacing is higher (about 4.6 GHz), thus providing a larger frequency range of stable operation for a mode near the frequency ω_g. Due to this fact, we also expect to have a larger tuning range from the onset of instability to the point where the laser jumps to a stable mode. We will analyze the evolution of different types of dynamical behavior as the mode is detuned through the region of instability. It is worth to note that $\hat{N}_c$ is about 1.5 in the scale of Fig. 9(a) for the current level of 80 mA, so the considered modes are well above threshold.

The mode to the right of the one indicated by the arrow in Fig. 9(a) is stable and has the normalized field power spectrum shown in Fig. 10. The small-signal spectrum derived from (49)

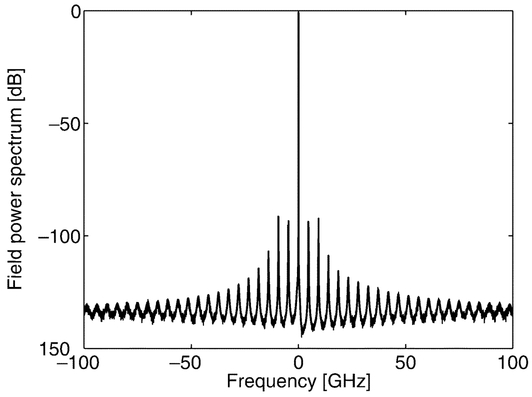

Fig. 10. Normalized field power spectra for the stable mode to the right of the mode highlighted in Fig. 9(a). The spectra, which are obtained from a small-signal analysis and from a time-domain simulation, can hardly be distinguished on the present scale. The figure demonstrates the ability of the time-domain approach to reproduce the spectral behavior over a large frequency range.

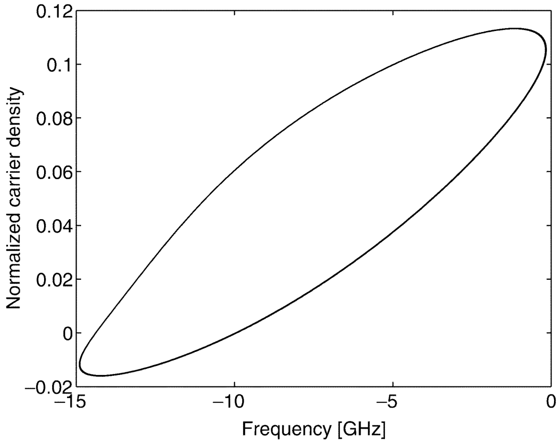

Fig. 11. Limit cycle in the carrier density vs frequency plane for the unstable mode of Fig. 9. The simulation was performed without spontaneous emission noise to get a clearer picture of the nonlinear dynamics.

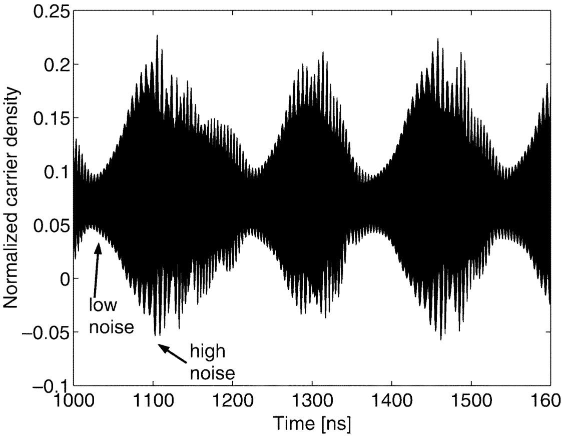

Fig. 12. Evolution of the unstable mode of Fig. 9 when its frequency is moved further into the instability region by varying the external cavity length. The chaotic behavior consists of a sequence of low and high amplitude noise fluctuations of the carrier density. Like in Fig. 11, the simulation was performed without spontaneous emission noise.

is again superimposed on the spectrum obtained from time-domain simulations. The two spectra show very good agreement over a large frequency scale.

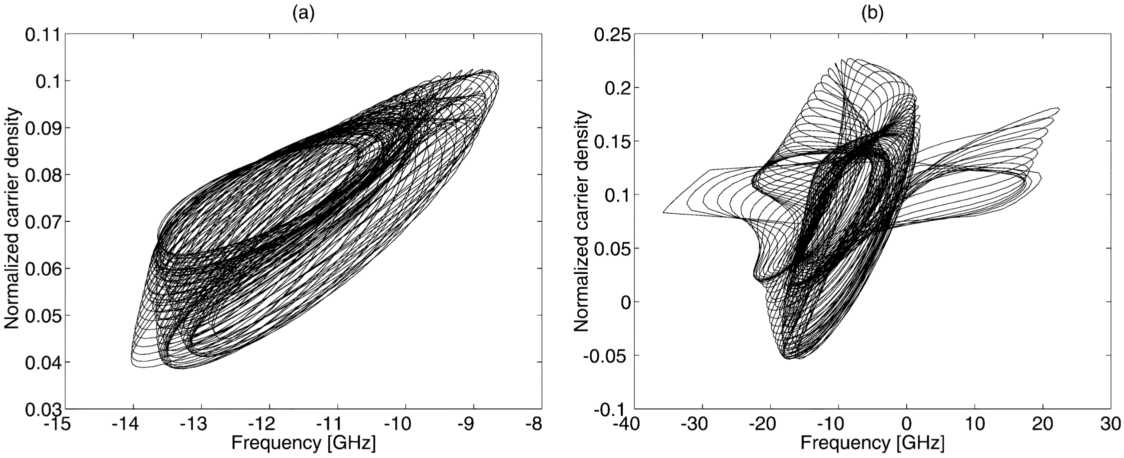

Fig. 13. Trajectories in the carrier density vs frequency plane for the two different low (a) and high (b) noise regions indicated in Fig. 12. The figures are shown with different axes limits to highlight the chaotic behavior in both cases.

We then move into the unstable region. The mode indicated by the arrow in Fig. 9(a) is found to be slightly unstable, having a side mode with negative imaginary frequency $(-2 \cdot 10^{-3}$ GHz); see Fig. 9(b). A time-domain simulation without noise gives in this case the limit cycle of Fig. 11 where the round-trip frequency equals the frequency of the undamped side mode (9.4 GHz).

Figs. 12 and 13 report the evolution of the stable limit cycle into chaotic behavior when the unstable mode is further tuned to lower frequencies along the locus curve of Fig. 9(a), by varying the length of the external cavity. The time evolution of the carrier density shows a slow periodic switching between low and high amplitude fluctuations (see Fig. 12), while Fig. 13 highlights the dynamical behavior in two different low and high noise regions, to give evidence of the chaos.

Finally, if the unstable mode is moved to even lower frequencies along the locus curve, it simply makes a mode hop to its neighboring mode [3]. This behavior is shown in Fig. 14, where the starting point of the time-domain simulation was chosen to be the mode to the left of the highlighted mode in Fig. 9(a). The time-domain trajectory (gray line) is plotted along with the locus curve to show the correspondence between the statically predicted position of the ECL modes and the actual transient dynamics. The time-dependent frequency was determined as the average $(\phi(t) - \phi(t-\tau))/2\pi\tau$, where $\phi(t)$ is the phase of $E(t)$ in (30).

In summary, a low selectivity of the external grating can provide an instability region for a mode on the locus curve, where no mode hops occur but the dynamical behavior ranges from a limit cycle to chaos.

V. CONCLUSION

We have illustrated the use of complex frequency diagrams to analyze the stability of an ECL with frequency-filtered feedback to a nonideal AR-coated laser facet. The analysis allows us to draw maps of stable single-mode operation in the current-detuning plane, similar to those obtained by Godard *et al.* [8] by an alternative method and shown to be in good agreement with experiments. The analysis may be used to provide guidelines for designing new single-mode devices. The latter requires a systematic parameter analysis, which is outside the scope of this paper.

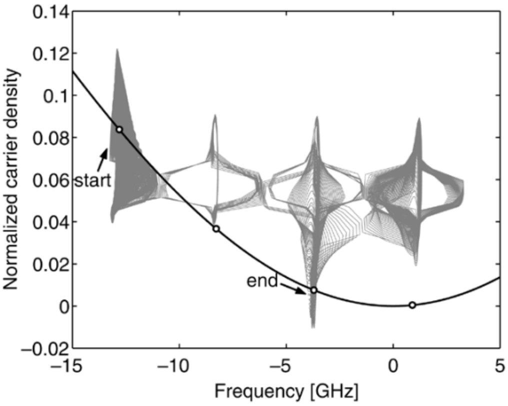

Fig. 14. Mode hops as time evolves (gray curve) when the ECL simulation is performed with the starting conditions of a mode deeply located in the unstable region and without spontaneous emission noise to better understand the dynamics. The locus curve (thick black curve with bullets as modes) is plotted over the time-domain trajectory to compare the exact theoretical position of the modes with the time-domain evolution.

We have also introduced a time-domain model for the electric field, which is a powerful tool to study the dynamics of both stable and unstable modes over a large range of frequencies. For stable modes, the time-domain simulations lead to noise spectra (relative intensity noise, frequency noise and field power spectra), which are in very good agreement with the corresponding spectra obtained from a small-signal analysis. The agreement holds over a frequency range of more than 200 GHz. The derivation of the small-signal field power spectrum requires a careful elimination of divergent terms.

Finally, we have exemplified the use of the time-domain model to study the nonlinear dynamics, which occur outside the region of stable operation. The examples show nonlinear phenomena (limit cycle, chaotic behavior, mode-hopping), which are familiar from other types of feedback systems. The simplicity of the model should make it attractive for a detailed mapping of the conditions under which the various types of nonlinear phenomena occur.

APPENDIX

In this appendix, we derive the expressions for the noise spectra when the ECL is operating in a stable mode $(\hat{\omega}_s, \hat{N}_s, E_s)$. We write the solution to (19) in the form

$$E(t) = E_s(1+\rho(t))e^{j(\hat{\omega}_s t + \phi(t))} \tag{30}$$

where $\rho(t)$ and $\phi(t)$ are real. In a small-signal analysis, they describe the amplitude and phase noise to first order in the Langevin noise function $F(t)$. The small-signal function $\delta E(\tilde{\omega})$ in (20) is the Fourier transform of $E_s(\rho(t)+j\phi(t))$, i.e.,

$$E_1 = \delta E(\tilde{\omega}) = E_s\left(\rho(\tilde{\omega}) + j\phi(\tilde{\omega})\right). \tag{31}$$

For simplicity, we use the same symbols ρ and ϕ in the time and frequency domain and distinguish between the domains by the argument of the functions. Their relations to E_1 and E_2 of (28) are

$$\rho(\tilde{\omega}) = \frac{1}{2}\left(E_1(\tilde{\omega}) + E_2(\tilde{\omega})\right) \quad \phi(\tilde{\omega}) = \frac{1}{2j}\left(E_1(\tilde{\omega}) - E_2(\tilde{\omega})\right). \tag{32}$$

The noise spectra are calculated from (28) and the correlation relations for the Langevin noise function $\mathcal{F}(\omega)$ of the field equation (2). The function describes the amplified spontaneous emission that is added to the field during one round trip in the open diode cavity which is confined by the left facet and the reference plane. It must, therefore, satisfy the correlation relations

$$\begin{aligned}\langle \mathcal{F}(\omega)\mathcal{F}^*(\omega')\rangle &= S_{\text{sp}}(\omega) 2\pi\delta\left(\omega-\omega'\right)\\ \langle \mathcal{F}(\omega)\mathcal{F}(\omega')\rangle &= \langle \mathcal{F}^*(\omega)\mathcal{F}^*(\omega')\rangle = 0\end{aligned} \tag{33}$$

where "$\langle\rangle$" denotes ensemble averaging. $S_{\text{sp}}(\omega)$ is the spectrum of amplified spontaneous emission from the open cavity with reflection from the left facet and no reflection from the right facet. For a uniform modal gain g, the spectrum becomes

$$S_{\text{sp}}(\omega) = \hbar\omega \frac{g n_{\text{sp}}}{g_{\text{net}}}(G-1)\left(1+r_1^2 G\right). \tag{34}$$

Here, $g_{\text{net}} = g - \alpha_i$ is the net modal gain, i.e., the modal gain g minus the internal loss α_i, n_{sp} is the population inversion factor, and $G = \exp(g_{\text{net}}\ell)$ is the total one-way gain. The form (34) is the familiar expression for the amplified spontaneous emission spectrum except for the factor $\left(1+r_1^2 G\right)$, which takes into account that the spontaneous emission moving left is reflected at the left mirror and is amplified as it moves to the right. From (33), we find that

$$\lim_{T\to\infty} \frac{1}{T}\langle \mathcal{F}(\omega)\mathcal{F}^*(\omega)\rangle = S_{\text{sp}}(\omega) \tag{35}$$

where the Fourier transform $\mathcal{F}(\omega)$ is taken over a finite time period T.

From (28), (32), (33), and (35), we obtain the following expressions for the relative intensity noise spectrum $\text{RIN}(\tilde{\omega})$ and the frequency noise spectrum $S_{\dot{\phi}}(\tilde{\omega})$:

$$\begin{aligned}\text{RIN}(\tilde{\omega}) &= 4\lim_{T\to\infty}\frac{1}{T}\langle|\rho(\tilde{\omega})|^2\rangle\\ &= \frac{S_{\text{sp}}(\omega_s+\tilde{\omega})|X'|^2 + S_{\text{sp}}(\omega_s-\tilde{\omega})|X|^2}{|E_s D|^2}\end{aligned} \tag{36}$$

and

$$\begin{aligned}S_{\dot{\phi}}(\tilde{\omega}) &= \lim_{T\to\infty}\frac{1}{T}\langle|\phi(\tilde{\omega})|^2\rangle\tilde{\omega}^2\\ &= \frac{\tilde{\omega}^2}{4|E_s D|^2}\left(S_{\text{sp}}(\omega_s+\tilde{\omega})|X'+2B'|^2\right.\\ &\qquad \left.+S_{\text{sp}}(\omega_s-\tilde{\omega})|X+2B|^2\right).\end{aligned} \tag{37}$$

The derivation of the field power spectrum $S_E(\tilde{\omega})$ is more complicated because we have to cope with the low-frequency divergence of the phase noise spectrum and the phase-amplitude cross-correlation spectrum caused by phase diffusion. The spectrum is defined as the Fourier transform

$$S_E(\tilde{\omega}) = \int_{-\infty}^{\infty} R_s(\tau)e^{-j\tilde{\omega}\tau}d\tau \tag{38}$$

of the autocorrelation function

$$\begin{aligned}R_s(\tau) &= \langle E^*(t)E(t+\tau)\rangle e^{-j\hat{\omega}_s\tau}\\ &\simeq E_s^2\langle(1+\rho(t)+\rho(t+\tau)+\rho(t)\rho(t+\tau))\,e^{j\Delta\phi}\rangle\end{aligned} \tag{39}$$

where

$$\Delta\phi = \phi(t+\tau) - \phi(t). \tag{40}$$

We shall approximate R_s by

$$\begin{aligned}R_s(\tau) = E_s^2\langle 1 + j(\rho(t)+\rho(t+\tau))\Delta\phi\\ +\rho(t)\rho(t+\tau)\rangle\langle e^{j\Delta\phi}\rangle.\end{aligned} \tag{41}$$

The approximation includes the effect of amplitude-phase cross correlation and the exponential ensures that the effect of phase diffusion is included to higher order in the spontaneous emission rate. However, in order to determine R_s correctly even to first order in the spontaneous emission rate, we would have to calculate ρ and ϕ to second order in $\mathcal{F}$.

The factor $\langle\exp(j\Delta\phi)\rangle$ is given by the familiar expression (see [18, eq. 6.5.45])

$$\langle e^{j\Delta\phi}\rangle = \exp\left(-\frac{\tau^2}{2\pi}\int_0^{\infty} S_{\dot{\phi}}(\omega)\frac{\sin^2\left(\frac{\omega\tau}{2}\right)}{\left(\frac{\omega\tau}{2}\right)^2}d\omega\right). \tag{42}$$

Its Fourier transform may be approximated by

$$\int_{-\infty}^{\infty}\langle e^{j\Delta\phi}\rangle e^{-j\tilde{\omega}\tau}d\tau \simeq L(\tilde{\omega}) + \frac{1}{\tilde{\omega}^2}\left(S_{\dot{\phi}}(\tilde{\omega}) - \frac{2}{\tau_{\text{coh}}}\right) \tag{43}$$

where $2/\tau_{\text{coh}} = S_{\dot{\phi}}(0)$, and $L(\tilde{\omega})$ is the Fourier transform of $\exp(-|\tau|/\tau_{\text{coh}})$, i.e., the Lorentzian

$$L(\omega) = \frac{2\tau_{\text{coh}}}{(\tau_{\text{coh}}\tilde{\omega})^2+1}. \tag{44}$$

τ_{coh} is the coherence time, and $1/(\pi\tau_{\text{coh}})$ is the spectral linewidth.

By (38), (41), and (43), the field power spectrum is given by the frequency-domain convolution

$$\begin{aligned}S_E(\tilde{\omega}) \simeq E_s^2&\left(2\pi\delta(\tilde{\omega}) + S_{\rho\phi}(\tilde{\omega}) + \frac{1}{4}\text{RIN}(\tilde{\omega})\right)\\ &\otimes\left(L(\tilde{\omega}) + \frac{1}{\tilde{\omega}^2}\left(S_{\dot{\phi}}(\tilde{\omega}) - \frac{2}{\tau_{\text{coh}}}\right)\right)\end{aligned} \tag{45}$$

where $S_{\rho\phi}(\tilde{\omega})$ is the amplitude-phase cross correlation

$$S_{\rho\phi}(\tilde{\omega}) = \lim_{T\to\infty} \frac{2}{T}\mathrm{Im}\langle \rho(\tilde{\omega})\phi^*(\tilde{\omega})\rangle. \tag{46}$$

The spectrum $S_{\rho\phi}(\tilde{\omega})$ diverges as $1/\tilde{\omega}$ as $\tilde{\omega} \to 0$, i.e.,

$$a = \lim_{\tilde{\omega}\to 0} \tilde{\omega} S_{\rho\phi}(\tilde{\omega}) \tag{47}$$

is finite. The function $S_{\rho\phi}(\tilde{\omega}) - a/\tilde{\omega}$ is, therefore, finite at $\tilde{\omega} = 0$. The linewidth of the mode is usually much smaller than the linewidths of the side modes, and $L(\tilde{\omega})$ will, therefore, to a good approximation act as a delta-function when convoluted with $S_{\rho\phi}(\tilde{\omega}) - a/\tilde{\omega}$ and $\mathrm{RIN}(\tilde{\omega})$. The convolution of $L(\tilde{\omega})$ with $a/\tilde{\omega}$ is the principal value integral

$$\frac{P}{2\pi}\int_{-\infty}^{\infty} L(\tilde{\omega}-\omega)\frac{a}{\omega}d\omega = \frac{a\tilde{\omega}{\tau_{\mathrm{coh}}}^2}{(\tilde{\omega}\tau_{\mathrm{coh}})^2+1}. \tag{48}$$

The convolution of $S_{\rho\phi}(\tilde{\omega}) - a/\tilde{\omega}$ and $\mathrm{RIN}(\tilde{\omega})$ with the phase noise term in (45) is of second order in the spontaneous emission rate and may be ignored. With these approximations, the expression for the field power spectrum finally reads

$$\begin{aligned} S_E(\tilde{\omega}) = E_s^2 \Bigg(L(\omega) &+ \lim_{T\to\infty}\frac{\langle |E_1|^2\rangle}{TE_s^2} \\ &- \frac{2}{\tilde{\omega}^2\tau_{\mathrm{coh}}} - \frac{a}{\tilde{\omega}((\tilde{\omega}\tau_{\mathrm{coh}})^2+1)}\Bigg) \end{aligned} \tag{49}$$

where

$$\begin{aligned} \lim_{T\to\infty}\frac{\langle |E_1|^2\rangle}{TE_s^2} &= \frac{1}{4}\mathrm{RIN}(\tilde{\omega}) + S_{\rho\phi}(\tilde{\omega}) + \frac{S_{\dot{\phi}}(\tilde{\omega})}{\tilde{\omega}^2} \\ &= \frac{S_{\mathrm{sp}}(\omega_s+\tilde{\omega})|X'+B'|^2 + S_{\mathrm{sp}}(\omega_s-\tilde{\omega})|B|^2}{|E_s D|^2}. \end{aligned} \tag{50}$$

The expression (49) is finite at $\tilde{\omega} = 0$, and it has the expected behavior for large $\tilde{\omega}$. If the contribution from nonlinear gain is ignored, the mode coupling parameter B and the reflectivity r_3 go to zero for $\tilde{\omega}$ larger than the carrier and reflector bandwidths. Hence

$$S_E(\tilde{\omega}) = \frac{S_{\mathrm{sp}}(\omega_s+\tilde{\omega})}{|1-r_2 r_L(\omega_s+\tilde{\omega}, N_s, P_s)|^2} \tag{51}$$

for large $\tilde{\omega}$, which is the subthreshold spectral behavior.

For uniform modal gain, the relation between the steady-state photon number P_s and $|E_s|^2$ is

$$P_s = \frac{(G-1)\left(1+r_1^2 G\right)}{\hbar\omega v_g r_1^2 g_{\mathrm{net}} G^2}|E_s|^2 \tag{52}$$

which implies that

$$\begin{aligned} \frac{S_{\mathrm{sp}}(\omega_s)}{4|E_s|^2} &= \frac{g n_{\mathrm{sp}}\tau_{\mathrm{in}}^2}{4Pv_g}\left(\frac{(G-1)\left(1+r_1^2 G\right)}{r_1 g_{\mathrm{net}} G\tau_{\mathrm{in}}}\right)^2 \\ &\simeq \frac{v_g g n_{\mathrm{sp}}\tau_{\mathrm{in}}^2}{4P_s}\left(\frac{(1-r_1 r_m)(r_1+r_m)}{2r_1 r_m \ln(r_1 r_m)}\right)^2. \end{aligned} \tag{53}$$

In the last step, $r_1 r_m G \simeq 1$ was used. The factor $v_g g n_{\mathrm{sp}}$ is the rate of spontaneous emission into the lasing mode, and the factor with the large parenthesis is the longitudinal Petermann factor (e.g., see [21, eq. 81]) which gives a noise enhancement for low Q cavities.

In the time-domain simulations, we ignore the frequency dependence of the spontaneous emission spectrum, and we use the ratio (53) in the expressions for the noise spectra.

ACKNOWLEDGMENT

The authors wish to thank J. Mørk of Research Center COM for stimulating discussions on lasers with optical feedback, and P. Bardella of Politecnico di Torino for important help on numerical processing techniques for the evaluation of noise spectra.

REFERENCES

[1] G. H. M. van Tartwijk and D. Lenstra, "Semiconductor lasers with optical injection and feedback," *Quantum Semiclass. Opt.*, vol. 7, pp. 87–143, 1995.

[2] D. Lenstra and B. Krauskopf, Eds., *Nonlinear Dynamics in Semiconductor Lasers*. New York: Plenum, 2000.

[3] A. M. Akul'shin *et al.*, "Anomalously wide continuous tuning range of the emission of an injection laser with an external selective resonator," *Sov. J. Quantum Electron.*, vol. 16, pp. 912–918, 1986.

[4] B. Tromborg, H. Olesen, X. Pan, and S. Saito, "Transmission line description of optical feedback and injection locking for Fabry–Perot and DFB lasers," *IEEE J. Quantum Electron.*, vol. QE-23, no. 11, pp. 1875–1889, Nov. 1987.

[5] J.-D. Park, D.-S. Seo, and J. G. McInerney, "Self-pulsations in strongly coupled asymmetric external cavity semiconductor lasers," *IEEE J. Quantum Electron.*, vol. 26, no. 8, pp. 1353–1362, Aug. 1990.

[6] P. Zorabedian, "Axial-mode instability in tunable external-cavity semiconductor lasers," *IEEE J. Quantum Electron.*, vol. 30, no. 7, pp. 1542–1552, Jul. 1994.

[7] A. P. A. Fischer, O. K. Andersen, M. Yousefi, S. Stolte, and D. Lenstra, "Experimental and theoretical study of filtered optical feedback in a semiconductor laser," *IEEE J. Quantum Electron.*, vol. 36, no. 3, pp. 375–384, Mar. 2000.

[8] A. Godard, G. Pauliat, G. Roosen, P. Graindorge, and P. Martin, "Side-mode gain in grating-tuned extended-cavity semiconductor lasers: Investigation of stable single-mode operation conditions," *IEEE J. Quantum Electron.*, vol. 38, no. 4, pp. 390–401, Apr. 2002.

[9] A. P. A. Fischer, M. Yousefi, D. Lenstra, M. W. Carter, and G. Vemuri, "Filtered optical feedback induced frequency dynamics in semiconductor lasers," *Phys. Rev. Lett.*, vol. 92, no. 023901, Jan. 2004.

[10] A. P. Bogatov, P. G. Eliseev, and B. N. Sverlov, "Anomalous interaction of spectral modes in a semiconductor laser," *IEEE J. Quantum Electron.*, vol. 11, no. 11, pp. 510–515, Nov. 1975.

[11] R. F. Kazarinov, C. H. Henry, and R. A. Logan, "Longitudinal mode self-stabilization in semiconductor lasers," *J. Appl. Phys.*, vol. 53, pp. 4631–4644, 1982.

[12] A. P. Bogatov, P. G. Eliseev, O. G. Okhotnikov, M. P. Rakhval'skii, and K. A. Khairetdinov, "Interaction of modes and self-stabilization of single-frequency emission from injection lasers," *Sov. J. Quantum Electron.*, vol. 13, pp. 1221–9, 1983.

[13] B. Tromborg, J. Mørk, and V. Velichansky, "On mode coupling and low-frequency fluctuations in external-cavity laser diodes," *Quantum Semiclass. Opt.*, vol. 9, pp. 831–851, 1997.

[14] A. P. Bogatov, P. G. Eliseev, O. A. Kobildzhanov, and V. R. Madgazin, "Suppression and spectral splitting of the amplitude noise due to mode beatings in a single-frequency injection laser," *IEEE J. Quantum Electron.*, vol. QE-23, no. 6, pp. 1064–1070, Jun. 1987.

[15] M. P. van Exter, R. F. M. Hendriks, J. P. Woerdman, and C. J. van der Pol, "Explanation of double-peaked intensity noise spectrum of an external-cavity semiconductor laser," *Opt. Commun.*, vol. 110, pp. 137–140, 1994.

[16] R. Ries and F. Sporleder, "Low frequency instabilities of laser diodes with optical feedback," in *Proc. 8th ECOC*, 1982, pp. 285–290.

[17] J. Mørk, B. Tromborg, and P. L. Christiansen, "Bistability and low-frequency fluctuations in semiconductor lasers with optical feedback: A theoretical analysis," *IEEE J. Quantum Electron.*, vol. 24, no. 2, pp. 123–133, Feb. 1988.

[18] G. P. Agrawal and N. K. Dutta, *Semiconductor Lasers*. New York: Van Nostrand Reinhold, 1995.

[19] H. Olesen, J. H. Osmundsen, and B. Tromborg, "Nonlinear dynamics and spectral behavior for an external cavity laser," *IEEE J. Quantum Electron.*, vol. QE-22, no. 6, pp. 762–773, Jun. 1986.

[20] Z. Ahmed and R. S. Tucker, "Small-signal IM response of grating-terminated external cavity semiconductor lasers," *IEEE J. Select. Topics Quantum Electron.*, vol. 1, no. 2, pp. 505–515, Jun. 1995.

[21] C. Henry, "Theory of spontaneous emission noise in open resonators and its application to lasers and optical amplifiers," *IEEE J. Lightwave Technol.*, vol. LT-4, no. 3, pp. 288–297, Mar. 1986.

Enrico Detoma was born in Biella, Italy, in 1975. He received the M.S. degree in electronic engineering from the Politecnico di Torino, Torino, Italy, in 2001, where he is currently working toward the Ph.D. degree in electronic and communication engineering.

His research interests include modeling and design of external cavity semiconductor lasers and theoretical investigation of the effects of optical feedback.

Bjarne Tromborg was born in 1940 in Give, Denmark. He received the M.Sc. degree in physics and mathematics from the Niels Bohr Institute, Copenhagen, Denmark, in 1968.

He was a university researcher studying high-energy particle physics and for one year was a high school teacher, until he joined the research laboratory of the Danish Teleadministrations, Copenhägen, Denmark, in 1979. He was Head of Optical Communications Department at Tele Danmark Research, Horsholm, Denmark (1987–1995), Adjunct Professor at the Niels Bohr Institute (1991–2001), Project Manager in Tele Danmark R&D, Taastrup, Denmark (1996–1998), and took a leave of absence at the Technion, Haifa, Israel, in 1997. He is now Research Professor in modeling of components and systems for optical communications at Research Center COM, Technical University of Denmark, Lyngby. He has coauthored a research monograph and more than 100 journal and conference publications, mostly on physics and technology of optoelectronic devices.

Prof. Tromborg was the recipient of the Electro-prize from the Danish Society of Engineers in 1981. He was Chairman of the Danish Optical Society from 1999 to 2002. He has been Associate Editor of the IEEE JOURNAL OF QUANTUM ELECTRONICS since 2003

Ivo Montrosset (M'92) was born in Aosta, Italy, in 1946. He received the Laurea degree in electronic engineering from the Politecnico di Torino, Torino, Italy, in 1971.

From 1972 to 1986, he was with the Politecnico di Torino. In 1986, he was appointed Full Professor at the Universita di Genova, Genova, Italy. Since 1990, he has been Full Professor of Optoelectronics at Politecnico di Torino. His main activities are in the field of guided wave-optics, solid-state and semiconductor lasers, and related topics.

Prof. Montrosset is a member of IEEE Lasers and Electro-Optics Society (LEOS) and of the Optical Society of America (OSA).